SUPPLEMENTAL FIGURES LEGENDS AND MOVIE CAPTIONS

Supplemental Figure 1. Quantification of membrane deformation from molecular dynamics simulations, related to Figure 3. (A) An example of the fitted two-dimensional Gaussian function (CGMD-eq-1) for a single frame from the antiparallel dimer simulation, pictured with contours. The protein is aligned horizontally, and mid-plane heights are depicted as points, colored by height. The fit shows significant negative curvature. (**B**) Visualization of the integrand of deformation energy. (**C**) Summary of induced curvature fields measured and computed from CGMD simulations. (**D**) An electrostatic map demonstrates the positive (blue) and negative (red) residues on the surface of Exo70. The membrane-contacting face of the protein interacts with both negatively-charged (DOPS, shown in yellow) and zwitterionic (DOPC, shown in blue) lipids in the bilayer. The figure shows all lipids bound within 12Å. (**E**) List of membrane-contacting residues that make persistent contacts with lipids. (**F**) Predicted number of proteins (“n”) required to induce tubular membranes for α=-0.6 and α=-1.0 for the various Exo70 systems.

Supplemental Figure 2. Characterization of Exo70-induced filopodia protrusions, related to Figure 4. (A) A B16F1 cell expressing GFP-Exo70, the box region was enlarged and lines were drawn perpendicular to the filopodia for fluorescence intensity measurements. Scale bar, 5 μm. **(B)** Fluorescence intensity profiles of lines 1-3 in (**A**) (dashed lines) and Gaussian fitting (solid lines). **(C)** The Full Widths at Half Maximum (FWHMs) were estimated from the Gaussian fitting. The ratios of GFP-Exo70 over actin signals for each line perpendicular to the protrusion were plotted, which are above 1 in all filopodia analyzed (n=20), usually higher in the distal region. **(D)** Exo70 was tagged by RFP-Ruby, a monomeric fluorescence protein. GFP-Lifeact was co-transfected with either RFP-Ruby-Exo70 or RFP-Ruby in B16F1 cells. Similar to GFP-Exo70, RFP-Ruby-Exo70 induced numerous protrusions. Scale bar, 5 µm. **(E)** GFP-Exo70 variants were expressed in B16F1 cells. The wild type Exo70 induced numerous filopodia. Exo70(Δ1-75) (oligomerization-defective) and Exo70(Δ628-630) (Arp2/3-binding-defective), though associated with the plasma membrane, failed to induce filopodia. GFP-Exo70(K571A/E572A) (PIP_2-binding-defective) did not associate with the plasma membrane. Scale bar, 10 µm. **(F-I)** Platinum replica EM samples of filopodia in B16F1 cells stably expressing GFP-Exo70. **(F)** Organization of actin filaments at the leading edge of a cell forming regular lamellipodia and filopodia. **(G)** Long and curvy filopodia found at the cell edge. **(H, I)** Enlarged views of boxed regions **h** and **i** from **G** showing loosely bundled actin filaments.

Supplemental Figure 3. Exo70-induced filopodia are independent of the other exocyst subunits, related to Figure 4. (A) GFP-Exo70 induced actin protrusions are independent of other exocyst subunits. B16F1 cells expressing GFP-Exo70 and siRNA targeting Sec8 or Sec15 were stained for F-actin and nuclei. Scale bar, 5 µm. The efficiency of siRNA treatment was examined by Western blotting. GFP-Exo70 induced approximately 20% of actin-free protrusions when Sec8 or Sec15 was depleted, similar to the control cells. In each treatment, 10 cells were counted. The total filopodia numbers are 1159 for control siRNA, 1038 for Sec8 siRNA and 1134 for Sec15 siRNA. **(B)** B16F1 cells treated with siRNA targeting Exo70, Sec8 or Sec15 were transfected with GFP or GFP-Cdc42L (see Figure 4G). The efficiencies of siRNA treatment were tested by Western blotting. **(C)** B16F1 cells were co-immunostained with mouse monoclonal antibody against endogenous Exo70 and rabbit polyclonal antibody against the exocyst subunit Exo84 (upper panel) or Sec10 (lower panel). The localization of Exo70 at the protruding plasma membrane was stronger than Exo84 or Sec10 in the same cell. Scale bars, 5 μm. **(D)** Quantification of the localization of different exocyst subunits at the protruding plasma membrane. The fluorescence intensities at the protruding plasma membrane and the whole cell were measured using ImageJ. Shown are the percentages of the leading edge intensities. Error bars, s.e.m; n=10; *, p<0.01. **(E)** Gel filtration of MDA-MB-231 cell lysates using a Superdex 200 10/300GL column in a buffer containing 20 mM HEPES, pH 7.4, 1 % NP-40, 100 mM KCl, 5 mM $MgCl_2$, 1 mM NaF, 1 mM DTT, 1mM PMSF. Fractions were collected and separated by SDS-PAGE and blotted for Sec8 and Exo70. Exo70 existed in a free pool (as indicated by "*", fraction 24-26) as well as the holo-complex that co-migrated with Sec8.

Supplemental Figure 4. Characterization of Exo70 mutants, related to Figure 6. (A) In vitro binding of wild type and mutant Exo70 with Sec8 (top left panel) and Sec6 (top right panel). Sec8 and Sec6 were in vitro transcribed and translated in the presence of [^{35}S] methionine using a TnT Quick Kit (Promega), and then incubated with GST-tagged Exo70 conjugated to glutathione Sepharose. The bound proteins were analyzed by SDS-PAGE and autoradiography (top panel). The gel was stained with Coomassie blue (lower panel). The GST-PreScission fusion protein was used as a negative control. **(B)** In vitro binding between Exo70 and Hisx6-Arpc1. Recombinant Hisx6-Arpc1 was incubated with GST-tagged Exo70 conjugated to glutathione Sepharose. The input (10%) and bound Hisx6-Arpc1 were analyzed by Western blotting using an anti-Hisx6 antibody (top panel).

Exo70 fusion proteins on the membrane were stained with Ponceau S. (lower panel). **(C-E)** VSV-G trafficking assay was performed as described previously (Liu et al., 2007). HeLa cells were transfected with Exo70 siRNA. Luciferase siRNA was used as a negative control. After 24 hours of siRNA treatment, HeLa cells were transfected with VSV-G-45ts-GFP mutant and FLAG-tagged rat Exo70 variants and immediately placed in a 40 ℃ incubator. After overnight growth, the cells were shifted to 32 ℃ for different times in the presence of cycloheximide (100 µg/ml). **(C)** Western blots showing Exo70 knockdown in HeLa cells and the expression of FLAG-tagged Exo70 variants. **(D)** Images of the cells at 0 min and 90 min after temperature shift showing total VSV-G-45ts-GFP (GFP signals, green), surface VSV-G-45ts-GFP (stained with 8G5 monoclonal antibody against the extracellular domain of VSV-G, red), and Exo70 variants expression (FLAG staining, blue). Scale bar, 5 µm. **(E)** The ratios of surface VSV-G over total VSV-G for each treatment at 0 min and 90 min. Depletion of Exo70 blocked surface incorporation of VSV-G-45ts-GFP, which were fully rescued by the wild type Exo70-FLAG and Exo70(Δ1-75)-FLAG, and only partially rescued by Exo70(K571A/E572A)-FLAG. Error bars, s.e.m. n=30; *, p<0.01. **(F)** The ability of the lysates from Exo70 knockdown cells expressing different Exo70 variants to stimulate actin polymerization was analyzed by pyrene actin assay in the presence of the VCA domain of N-WASP as described in Liu et al, 2009a. Lysates from Exo70 siRNA knockdown cells showed reduced actin polymerization. Expression of GFP-Exo70, GFP-Exo70(Δ1-75) and GFP-Exo70(K571A/E572A), but not GFP-Exo70(Δ628-630) (Arp2/3-binding-defective), rescued this phenotype induced by Exo70 siRNA. Actin polymerization rates (the maximal slops of the elongation phase of each curve) were compared after normalized to

GFP-Exo70 + Exo70 siRNA. GFP-Exo70(Δ1-75) had the same activity as GFP-Exo70 to stimulate actin polymerization. Error bars, s.e.m. n=4; *, $p < 0.01$. Endogenous and exogenous Exo70 levels were examined by Western blot, along with the amounts of actin in cell lysates.

Supplemental Figure 5. The function of Exo70 in membrane deformation is required for wound closure of cell monolayer, related to Figure 7. (A) Exo70 knockdown in MDA-MB-231 cells stably expressing GFP or GFP-tagged rat Exo70 variants. Control siRNA or Exo70 siRNA were transfected into MDA-MB-231 cells stably expressing GFP or GFP-tagged rat Exo70 variants including Exo70, Exo70(K571A/E572A), or Exo70(Δ1-75). The amounts of endogenous Exo70 and exogenously expressed various GFP-tagged rat Exo70 constructs were detected by anti-Exo70 monoclonal antibody. The expression of GFP was detected by anti-GFP monoclonal antibody. The amounts of actin in all treatments, detected by an anti-actin antibody, were also examined as loading controls. **(B)** Wound healing assay in Exo70 siRNA knockdown cells expressing various Exo70 mutants (in reference to Figure 7B). Control siRNA or Exo70 siRNA were transfected into MDA-MB-231 cells stably expressing GFP or GFP-tagged rat Exo70 variants including Exo70, Exo70(K571A/E572A), or Exo70 (Δ1-75). Cells were grown to confluence for wound-healing assays. Images were taken at 0, 6, 24, 48 hours after the open space (“wound”) was introduced. Red dashed lines indicate the leading edges of migrating cells. Scale bar, 100 μm.

Supplemental Movie 1. **Tilt series of an Exo70-deformed LUV (in reference to Figure 1B)**. Samples were prepared as described in Figure 1B and Experimental

Procedures. The specimens were tilted ±20 ° at 5 ° intervals and imaged. The images were aligned and reconstituted with TomoJ plugin in ImageJ for 3-D reconstruction, which shows the connectivity of the tubular invaginations induced by Exo70 with the exterior of the LUV. **1a** shows the LUV containing 30% PIP_2; **1b** shows the LUV containing 5% PIP_2. Scale bar, 100 nm.

Supplemental Movie 2(a-b). Representative snapshots from molecular dynamics simulations of Exo70 dimers (in reference to Figure 3A). The images were rendered in VMD showing comprehensive views. (a) anti-parallel dimer; (b) parallel dimer.

Supplemental Movie 3(a-e). Exo70 dimers induce negative curvature in lipid bilayer (in reference to Figure 3A). Molecular dynamics simulations were performed as described in Figure 3 and Supplemental Experimental Procedures. The movies depict frame-by-frame fits to the height of the mid-plane of the bilayer clearly demonstrating the recording of negative curvature in our simulations. (a) anti-parallel dimer; (b) parallel dimer; (c) Exo70(Δ1-75) monomer; (d) Exo70(K571A/E572A) dimer, and (e) no protein control.

Supplemental Figure 1

A

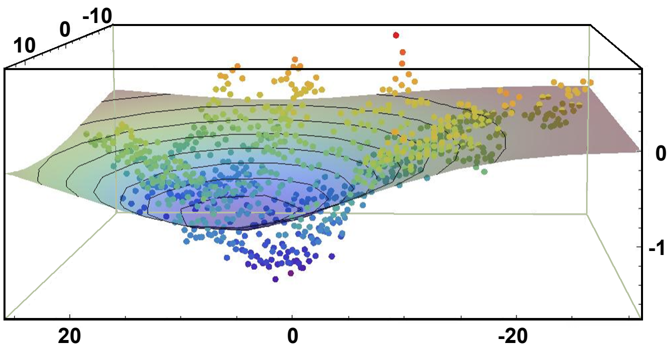

$$z(x,y) = A_0 \exp\left\{\frac{(x-x_0)^2}{2\sigma_x^2}\right\}\exp\left\{\frac{(y-y_0)^2}{2\sigma_y^2}\right\}$$

(CGMD-eq-1)

B

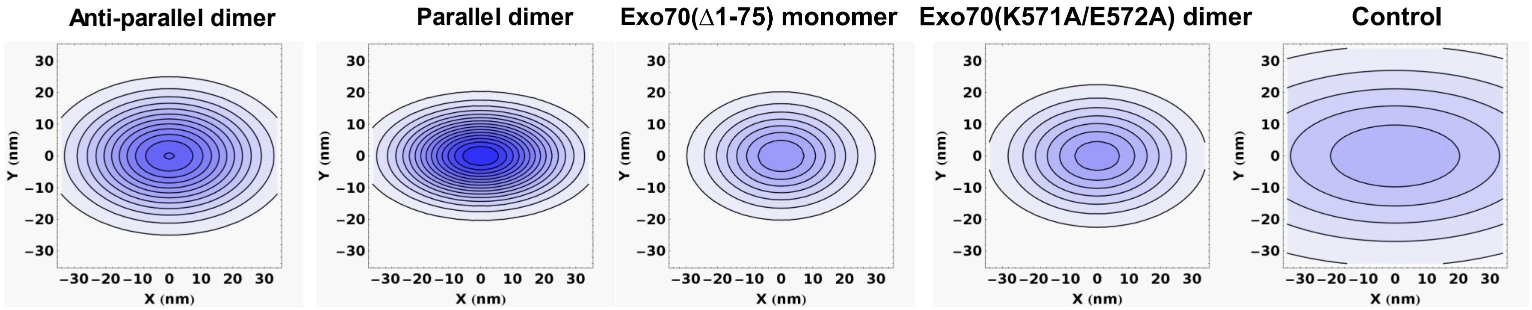

C

System	$\langle H_{max}\rangle$ (nm^{-1})	$\langle\sigma_x\rangle$ (nm)	$\langle\sigma_y\rangle$ (nm)	Radius (nm)	$\langle E\rangle=\iint\langle H\rangle^2 dxdy$
Anti-parallel dimer	-9.4×10^{-3}	11.2	17.4	53	0.0537
Parallel dimer	-12.4×10^{-3}	8.6	16.1	40	0.0667
Exo70(Δ1-75) monomer	-6.2×10^{-3}	9.9	14.6	81	0.0174
Exo70(K571A/ E572A) dimer	-5.9×10^{-3}	11.1	17.2	84	0.0208
Control	-4.4×10^{-3}	18.6	38.9	112	N/A

E

Position	Residue	Position	Residue
404	ASP	407	LYS
408	GLU	336	ARG
329	GLU	330	ASN
343	ASP	484	VAL
501	LYS	502	GLU

D

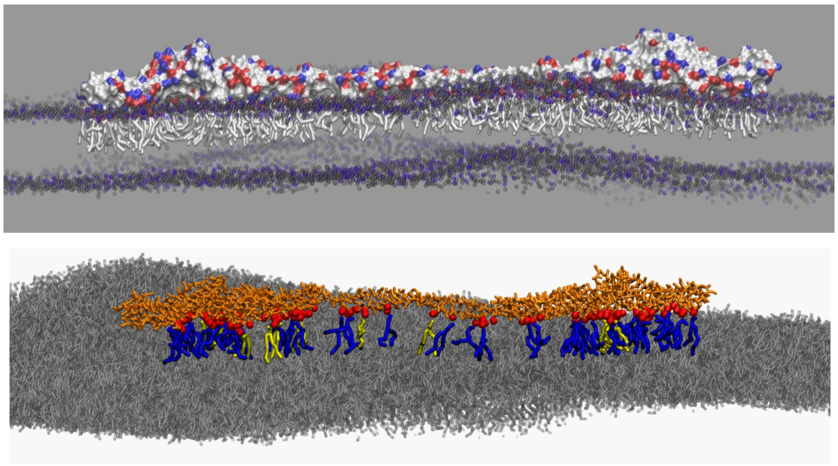

F

System	n (α = -0.6)	n (α = -1.0)	n*
Anti-parallel dimer	1.22	3.40	1.23
Parallel dimer	0.99	2.74	1.47
Exo70(Δ1-75) monomer	3.78	10.49	1.96
Exo70(K571A/ E572A) dimer	3.17	8.80	1.23

Supplemental Figure 2

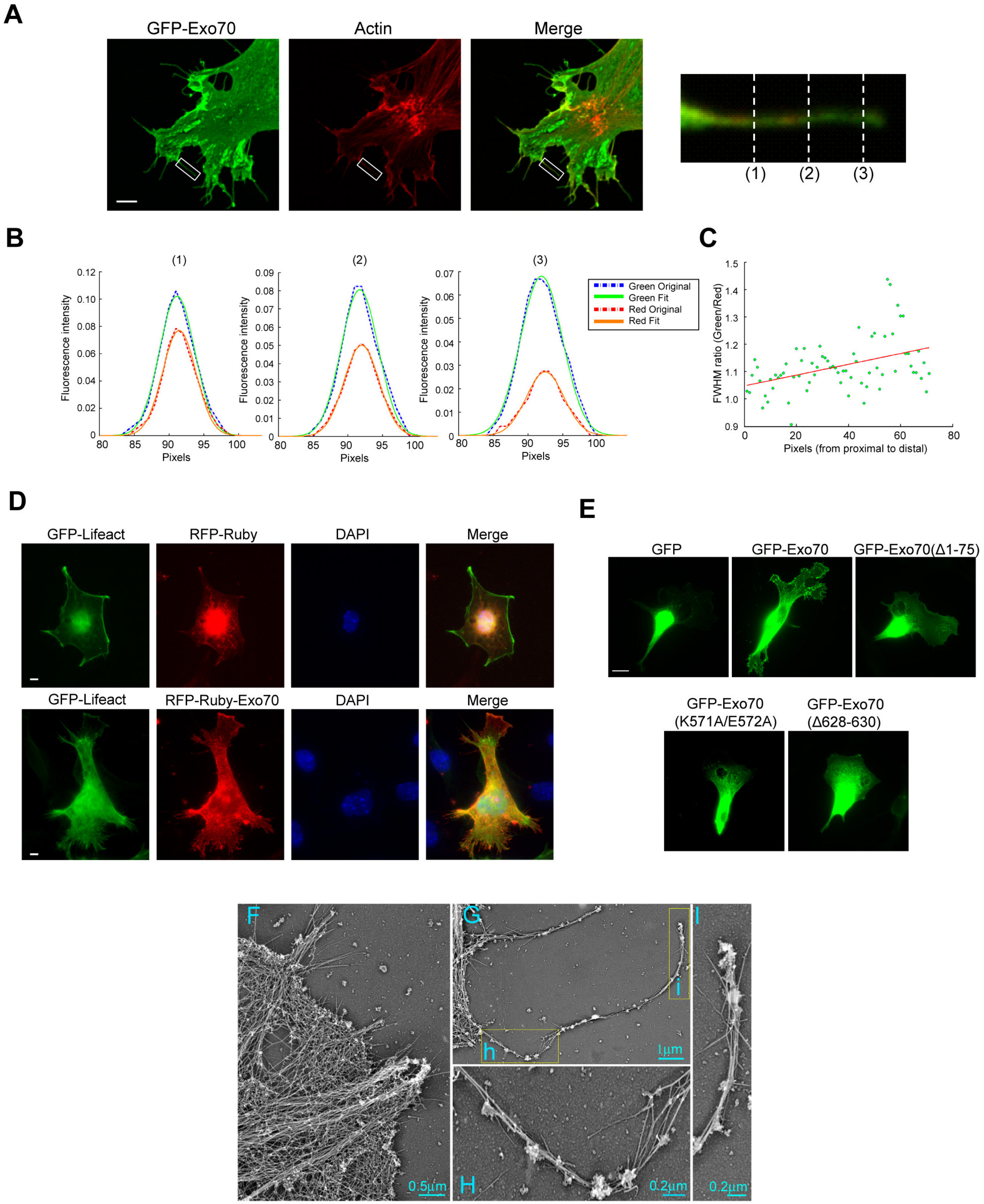

Supplemental Figure 3

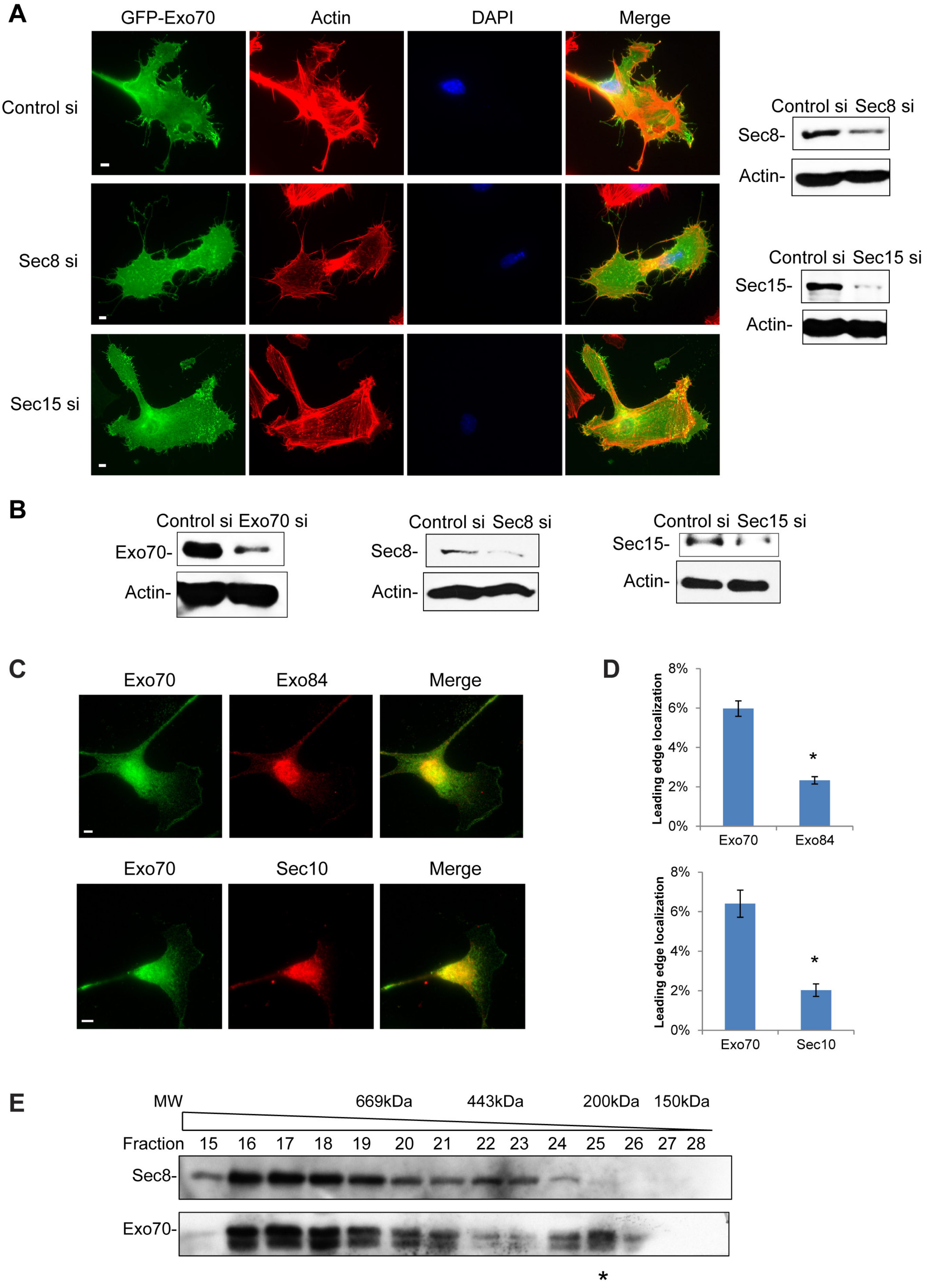

Supplemental Figure 4

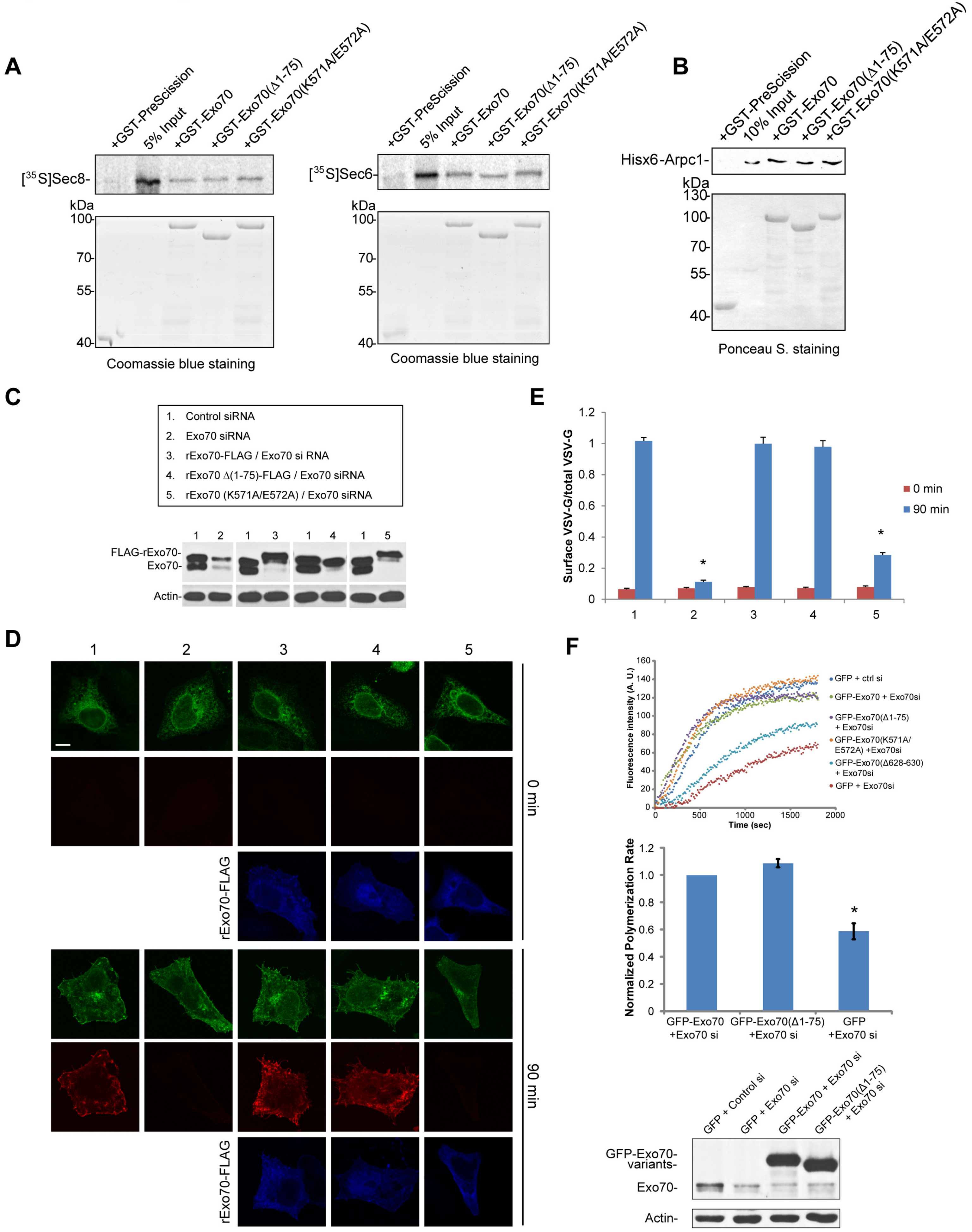

Supplemental Figure 5

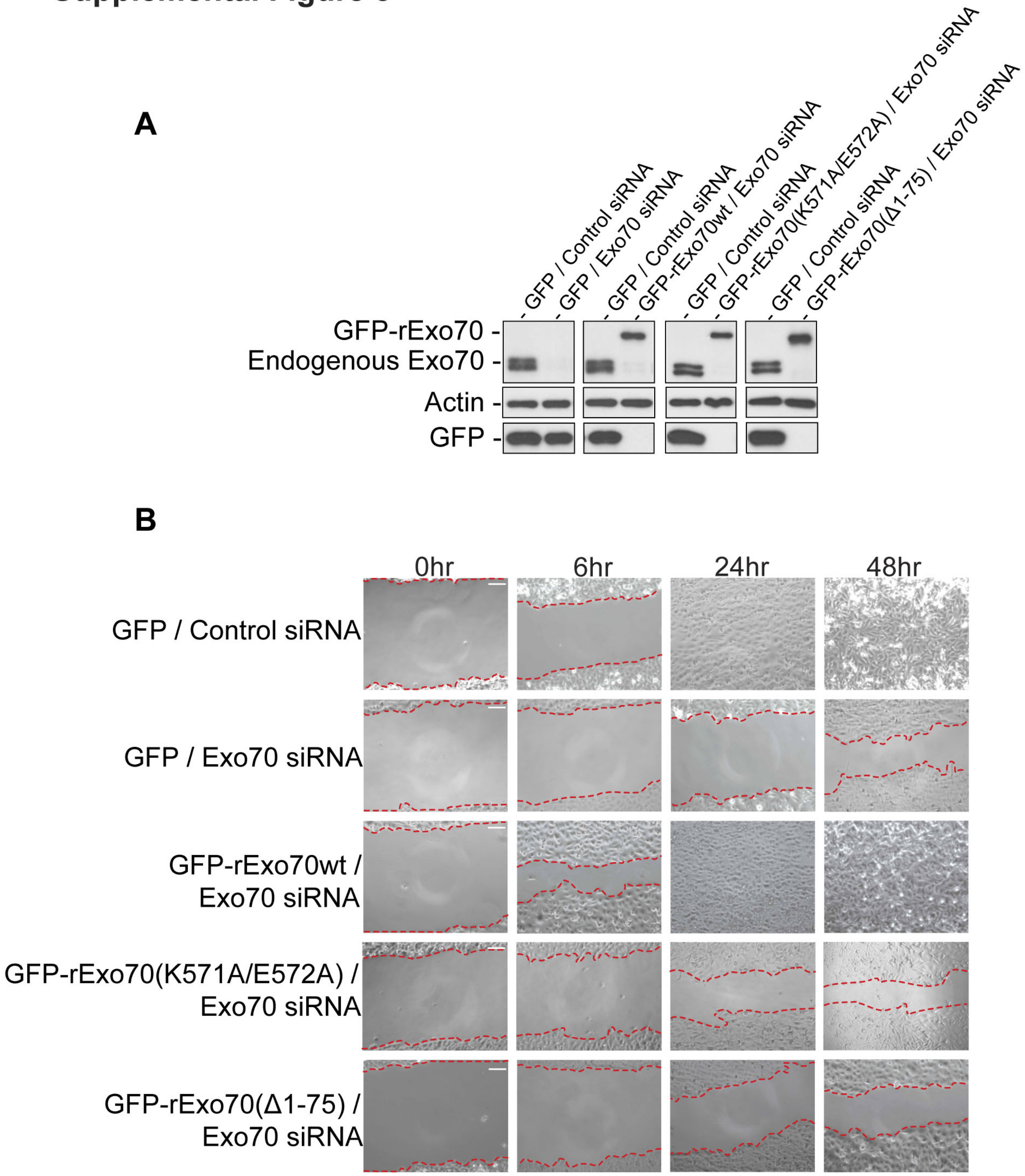

SUPPLEMENTAL EXPERIMENTAL PROCEDURES

Plasmids and antibodies

Full-length rat Exo70 and Exo70(Δ1–75) were cloned in-frame into pEGFP-C1 vector or p3xFLAG-CMV-14 vector for expression in cells. Full-length rat Exo70 was cloned in-frame into pJ3-RFP-Ruby for expression in cells. The Exo70 mutant Exo70(K571A/E572A) were generated using the QuikChange site-directed mutagenesis kit (Stratagene). Different Exo70 variants were also cloned in-frame into pGEX-KG (a modified form of pGEX-2T) or pGEX-6P-1 (GE Healthcare/ Amersham Biosciences) for bacterial expression. Mouse MIM-I-BAR (a.a.1-250) in vector pTYB12 was provided by Dr. Roberto Dominguez (University of Pennsylvania). Monoclonal antibodies against Sec8, Sec15, Exo70 were obtained from Dr. Shu-Chan Hsu (Rutgers University). Polyclonal antibody against Exo84 was obtained from Dr. Charles Yeaman (University of Iowa). Mouse anti-actin mAb (MAB 1501, clone C4) was purchased from Chemicon, Millipore; mouse monoclonal anti-Hisx6 antibody (NMS-118R) from Covance; monoclonal antibody against GFP (NMS-118R, clone B34), monoclonal antibody against FLAG (F3165, clone M2) was purchased from Sigma and polyclonal antibody against FLAG (A00170) was purchased from Genescript. The 8G5 monoclonal antibody against the extracellular domain of VSV-G was a kind gift from Dr. Douglas Lyles (Wake Forest University).

Protein purification

GST fusion proteins were expressed in *E. coli* strain BL21-CodonPlus(DE3)-RP and purified using glutathione Sepharose 4B (GE Healthcare). GST-tagged Exo70 fusion proteins were cleaved with PreScission protease to remove GST in 50 mM Tris-HCl, 150mM NaCl, 1mM EDTA, 1mM dithiothreitol (pH 7.0) overnight at 4℃; the resins were then washed with PBS containing 1mM DTT to elute the liberated recombinant proteins. MIM-I-BAR was purified as previously described (Lee et al., 2007). Briefly, chitin tagged MIM-I-BAR was incubated with chitin beads (New England Biolabs) in 20 mM Tris (pH 7.5), 500 mM NaCl, 1 mM EDTA, 100 μM PMSF. MIM-BAR was eluted from the beads following DTT-induced self-cleavage of the intein and dialyzed into the desired buffers. His6-Arpc1 was purified from *E. coli* with TALON beads.

Cell culture and transfection

MDA-MB-231 cells were maintained at 37℃ in DMEM (Invitrogen) supplemented with 10% FBS, 2 mmol/L l-glutamine, 100 U /ml penicillin, and 100 μg/ml streptomycin in a 5% CO_2 incubator. B16F1 mouse melanoma cells were maintained in DMEM/F12 (Invitrogen) supplemented with 10% FBS (Yang et al., 2007). DNA transfections into MDA-MB-231 cells were carried out using Lipofectamine 2000 (Invitrogen). DNA transfections into B16F1 cells were performed using Lipofectamine™ LTX with Plus™ Reagent (Invitrogen). For RNA interference (RNAi), cells were grown to 50% confluence and transfected with small interfering RNA (siRNA) duplexes using Lipofectamine 2000. The human Exo70 siRNA target sequence used in the experiments is 5’-GGTTAAAGGTGACTGATTA-3’. The control Luciferase GL2 siRNA target sequence is 5’-AACGTACGCGGAATACTTCGA-3’. The efficiency of the knockdown was determined by Western blotting. Stable MDA-MB-231 cell lines expressing GFP, GFP-tagged wild-type and mutant Exo70 were selected by G418 at a concentration of 1 mg/ml. The cells were further selected using fluorescence activated cell sorting (FACS) and maintained in growth medium for 2 weeks. B16F1 cell line stably expressing GFP-

Exo70 was generated using the same procedure as above except that the concentration of G418 for the selection of stable cell line is 1.6 mg/ml. The mouse Sec8 siRNA target sequence used is 5'-GTCCTGATGACAACTTAATTT-3'. The mouse Sec15 siRNA target sequences are 5'-AAAGATATCATTCGATGTAGA-3' and 5'-AACAAGTGACGGATACTAATA-3'.

Immunoprecipitation and in vitro binding assay

HEK293T cells co-expressing Exo70-FLAG and the following constructs: GFP-Exo70, GFP-Exo70(Δ1-75) or GFP vector were lysed in a buffer containing 50 mM Tris-HCl (pH 8.0), 135 mM NaCl, 1mM EDTA, 1 mM Va_3VO_4, 0.5% Triton X-100 and protease inhibitors. Cell lysates were incubated overnight with anti-Flag (M2) agarose (Sigma) at 4 ℃. The inputs and bound proteins were analyzed by Western blotting using an anti-GFP monoclonal antibody. The same membrane was stripped with Restore Western Blot Stripping Buffer (Thermo Scientific) and blotted with FLAG monoclonal antibody.

For in vitro binding assay, rat Sec8 and Sec6 were in vitro transcribed and translated in the presence of [^{35}S] methionine using a TnT Quick Kit (Promega), and then incubated with GST-tagged Exo70 variants conjugated to glutathione Sepharose 4B beads in binding buffer (50 mM Tris-HCl pH 8.0, 135 mM NaCl, 1mM EDTA, 1 mM Va_3VO_4, 0.5% Triton X-100). After overnight incubation at 4 ℃, beads were washed three times. The bound proteins were analyzed by SDS-PAGE and autoradiography. Recombinant Hisx6-Arpc1 was incubated with GST-tagged Exo70 variants as described above. The bound proteins were analyzed by Western blotting using an anti-Hisx6 antibody.

Characterization of curvature in CGMD simulations

To characterize the induced curvature from these CGMD simulations, we have modeled the height of the mid-plane of the bilayer as a two-dimensional anisotropic Gaussian function centered and oriented with respect to the location of the protein (see below). This method provides a general description of the induced curvature by separately measuring the position, extent, degree of anisotropy, magnitude of curvature of the associated lipids and fluctuations due to dynamics/membrane undulations.

Since Exo70 dynamically remodels the associated bilayer, it was necessary to analyze the average as well as the fluctuations about the average in bilayer curvature to deconvolute the curvature effect from the undulation modes of the bilayer. Specifically, we must distinguish between negative curvature induction and the random fluctuations in the height of the bilayer. To this end, we first constructed a surface corresponding to the mid-plane of the bilayer and aligned the protein along its principal axis in each frame of the simulation. Then, for each frame, we divided the bilayer mid-plane surface into 5×5 nm patches and considered the patches that were within 10 nm of any atom of the protein. Analysis of a control membrane with no associated protein indicates that this filter effectively removes local undulations, which add noise to our estimate of curvature without changing the overall result. That is, the measured curvature of our control simulation is effectively infinite. The heights of these relevant mid-plane patches were then fit (frame-by-frame, see Supplemental Movie 3) to a two-dimensional Gaussian function given by,

$$\mathrm{z(x,y)} = \mathrm{A_0}\exp\left\{\frac{(\mathrm{x}-\mathrm{x_0})^2}{2\sigma_\mathrm{x}^2}\right\}\exp\left\{\frac{(\mathrm{y}-\mathrm{y_0})^2}{2\sigma_\mathrm{y}^2}\right\}. \qquad \text{(CGMD-eq-1)}$$

Here, x and y are orthogonal axes chosen with respect to the alignment of the protein. The quantities σ_x and σ_y are the standard deviations in orthogonal directions, each corresponding to the "width" or extent of curvature of the fitted Gaussian parallel and perpendicular to the aligned axis of the protein. The maximum curvature is induced at the position (x_0, y_0) where the height is A_0 higher than the average. This position is not necessarily at the center of the protein. The fits to equation CGMD-eq-1 from the frames are depicted in Supplemental Movie 3, clearly showing negative curvature induced by the protein. Note that this fitting procedure is a conservative estimate of the negative curvature because it always predicts a curvature smaller than the actual curvature observed in the simulations.

We calculate the strength of the induced curvature according to the following expression for mean curvature,

$$H = \frac{\left(1+z_x^2\right)z_{yy}+\left(1+z_y^2\right) z_{xx} \; - 2z_x \, z_y \, z_{xy}}{\left(1+z_x^2+z_y^2\right)^{\frac{3}{2}}}. \text{(CGMD-eq-2)}$$

Here, z_{xy} terms correspond to the partial derivatives of the height of the fitted function. Thus, for each frame we have obtained a maximum mean curvature, i.e. $\mathrm{H}(\mathrm{x}_0,\mathrm{y}_0)$ from equation CGMD-eq-1, and values σ_x and σ_y which characterize the parallel and perpendicular extent of curvature, see Supplemental Figure 1A-C.

In order to esimate the average deformation induced by the protein on the membrane, we compute the average deformation energy $\langle \mathrm{E} \rangle$ (in units of κ) using the expression:

$$\langle E \rangle = \int_0^{\sigma_x} dx \int_0^{\sigma_y} dy \left[\langle H_{max} \rangle \exp\left\{ \frac{(x-x_0)^2}{2\langle \sigma_x^2 \rangle} \right\} \exp\left\{ \frac{(y-y_0)^2}{2\langle \sigma_y^2 \rangle} \right\} \right]^2. \qquad \text{(CGMD-eq-3)}$$

Here $\langle E \rangle$ represents the ensemble average over all the frames of the CGMD simulation; the average quantities and the integrand are summarized in Supplemental Figure 1B and C. These quantities are input into a mesoscale model (described below) in order to predict their effect on vesicle morphology.

Mesoscale Model

The physical properties of a biological membrane can be understood using a phenomenological model, the well-known being the Helfrich Hamiltonian given by,

$$\mathscr{H}_{\mathrm{el}} = \int dA \left\{ \frac{\kappa}{2} (H - H_0)^2 + 2\kappa' K + \sigma \right\}. \qquad (Mesoscale - 1)$$

Here, the membrane is approximated to a two dimensional fluid, elastic sheet, with lateral dimensions large enough to neglect its thickness. The phenomenological parameters, κ, κ' and σ are the bending rigidity, Gaussian rigidity and surface tension of the membrane, whose surface area is A. The gauge invariants $H = (c_1 + c_2) / 2$ and $K = c_1 c_2$ are respectively the mean and Gaussian curvature of the membrane, where c_1 and c_2 are the two principal radii of curvatures, and H_0 is the spontaneous curvature (magnitude of imposed deformation) imposed on the membrane by a curvature modulating factor, which in general denotes any heterogeneity in composition of the membrane. For a membrane with fixed topology and for constant κ', by virtue of the Gauss-Bonnet theorem, the Gaussian rigidity term remains a constant irrespective of the membrane morphology, and is hence not included in our studies using Monte Carlo methods.

In our model, the Exo70 proteins interacting with the membrane is represented by a nematic vector $\boldsymbol{n}$, which represents the orientation of proteins averaged over a small membrane patch, the size of which sets the smallest length scale a_0 in the mesoscopic model. The nematic field is representative of the anisotropic nature of the membrane deformation seen in the CGMD simulation. These nematic vectors interact among themselves leading to an orientational order in the nematic field. This self-interaction, promoting orientational order, is represented by the Lebwohl-Lasher form of the Frank's free energy for liquid crystals given by,

$$\mathscr{H}_{\text{nem}-\text{nem}} = \frac{1}{2}\sum_{v=1}^{N_v}\sum_{v'=1}^{Z_v} -\varepsilon_{LL}\left(3\cos^2\theta_{vv}^{'} - 1\right). \qquad (Mesoscale-2)$$

The first summation index v runs over all membrane vertices and v' runs over its Z_v neighboring vertices. ε_{LL} is the orientational stiffness and $\theta_{vv'}$ is the angle between $\boldsymbol{n}(\boldsymbol{v})$ and $\boldsymbol{n}(\boldsymbol{v}')$, computed on the curved manifold through a discrete parallel transport. $\boldsymbol{n}(\boldsymbol{v})$ is a two-dimensional unit vector confined to the surface of the membrane, as a protein does, and subtends an angle φ with the maximally curved direction of the membrane. We extend the Helfrich Hamiltonian, Eq. (Mesoscale-1), to include anisotropic curvature and account for the protein membrane interaction through an anisotropic energy term given by,

$$\mathscr{H}_{\text{nem}-\text{mem}} = \frac{1}{2}\sum_{v=1}^{N_v}\left\{\kappa_{\parallel}\left(c_1\cos^2\varphi + c_2\sin^2\varphi - H_0^{\parallel}\right)^2\right\}A_v\,. \quad (Mesoscale-3)$$

where $\kappa_{\parallel}(\kappa_{\perp})$ and $H_0^{\parallel}(H_0^{\perp})$ are respectively the anisotropic bending stiffness and anisotropic spontaneous curvature parallel (perpendicular) to the nematic field $\boldsymbol{n}$. This model has been earlier used (Ramakrishnan 2012; Ramakrishnan 2013) to demonstrate how biologically relevant membrane morphologies can be stabilized in response to the imposed curvature. The nematic field evolves through a set of Monte Carlo moves that sample the phase space of the system that spans over the membrane position, triangulation and nematic field orientations using the Metropolis algorithm. It should also be noted that the anisotropic curvature field is represented in units of a_0 such that $H_0^{\parallel} = \alpha a_0^{-1}$. The total energy of the membrane with nematic field is $\mathcal{H}_{\text{tot}} = \mathcal{H}_{\text{el}} + \mathcal{H}_{\text{nem}-\text{nem}} + \mathcal{H}_{\text{nem}-\text{mem}}$. For the set of elastic parameters $\kappa = 20 k_B T, \epsilon_{LL} = 3 k_B T$ and $\kappa_{\parallel} = 5 k_B T$ membrane invaginations are seen only for directional curvatures with $\alpha < -0.6$, see Figure 3 in main text. Below, we combine this result from the mesoscale model with the average membrane deformation energy $\langle E \rangle$ computed from the CGMD simulations (Supplemental Figure 1C) in order to predict the threshold protein density required to induce tubular invaginations (see Figure 3 and main text) for various Exo70 systems.

For an imposed value of $H_0^{\parallel}$, the nematic-membrane energy $\mathcal{H}_{\text{nem}-\text{mem}}$ is minimized when the directional curvature of the membrane is such that $c_1 \cos^2 \varphi + c_2 \sin^2 \varphi = H_0^{\parallel}$. Hence the mean curvature of the membrane at every vertex (H) and the energy per vertex E_{vertex} of the triangulated surface are given by:

$$H = \frac{H_0^{\parallel}}{2} = \frac{\alpha}{2a_0} \text{ and } E_{vertex} = \frac{1}{2}\left(\frac{H_0^{\parallel}}{2}\right)^2 A_v. \quad (Mesoscale - 4)$$

To account for the presence of multiple proteins (n) represented by the curvature field vector, we assume that the mean curvature energy $\langle E \rangle$ shown in Supplemental Figure 1C scales linearly with the number of proteins n. The minimum value of n per membrane area A_v necessary for inward-tubule invagination is estimated using the criterion $E_{\text{vertex}}=n\langle E \rangle$, where $A_v = \sqrt{3}(1.3a_0)^2/2$ is the average area of the vertex in units of a_0. The expression for n reduces to (see Supplemental Figure 1F):

$$n = \frac{\sqrt{3}(1.3)^2\alpha^2}{16\langle E \rangle}. \qquad (Mesoscale - 5)$$

The theoretical maximum value of the number of proteins n^* in area A_v is estimated as $n^* = (A_v = 294\ \text{nm}^2)$ / (molecular area). Based on the molecular areas of the different systems (monomer=150 nm^2, parallel dimer=200 nm^2, and anti-parallel dimer=240 nm^2), the value of n^* is estimated in Supplemental Figure 1F. Note that n is a parameter set for mesoscale simulations while the maximum number n* is based on CGMD simulations; if n<n*, inward-tubulation is predicted to occur and if n>n*, inward-tubulation is predicted not to occur. Hence, the computed numbers collectively imply that tubulation occurs only for the parallel and anti-parallel wild type dimer systems. Alternatively, noting that the anti-parallel dimer system barely satisfies the constraint n<n* (see Supplemental Figure 1F), we can estimate the critical radius of curvature $R^* = \langle 2H^*_{\text{max}} \rangle^{-1}$ as 53.4 nm. For systems with R>R*, we expect no tubulation and for systems with R<R*, we expect tubulation, again predicting that the wild type parallel (R=40 nm) and anti-parallel dimers (R=53 nm) are the only systems expected to stabilize

inward-tubulation. The different radii of curvature along with the threshold R* are depicted in Figure 3 of main text.

VSV-G trafficking assay

VSV-G trafficking assay was performed as described previously (Liu et al., 2007). HeLa cells were transfected with Exo70 siRNA. Luciferase siRNA was used as a negative control. After 24 hours of the siRNA treatment, HeLa cells were transfected with VSV-G-45ts-GFP mutant and FLAG-tagged Exo70 variants and immediately placed at 40 ℃. After overnight growth, the cells were shifted to 32 ℃ for different times in the presence of cycloheximide (100µg/ml). The cells were then fixed for GFP observation and immunofluorescence using the 8G5 mAb against the extracellular domain of VSV-G without cell permeabilization. Subsequently, cells were permeabilized and stained with anti-FLAG polyclonal antibody to detect the expression of transfected FLAG-tagged Exo70. Anti-mouse Alexa488 and anti-rabbit Alexa633 were used as secondary antibodies in these experiments. Images were obtained using Leica DMI 6000B inverted microscope equipped with a DFC350 FX camera and a 63x objective. Surface VSV-G intensity (8G5 signal) and total VSV-G intensity (GFP signal) were measured by ImageJ software. Three independent experiments were carried out. 30 cells were analyzed for each treatment.

Pyrene actin assay

Pyrene actin assay was performed as described in Liu et al., 2009a. Cell lysates were collected in a buffer containing 20 mM Tris-HCl, pH 7.5, 25 mM KCl, 1 mM $MgCl_2$, 0.5 mM EGTA, 0.1 mM ATP, and protease inhibitor cocktail [Sigma P8340, 4-(2-aminoethyl) benzenesulfonyl fluoride, pepstatin A, E-64, bestatin, leupeptin, and aprotinin], and 1 mM DTT and spun successively at 16,000 × g for 15 min and 80,000 rpm in a Beckman TLA-100.3 rotor (Fullerton, CA) for 20 min at 4 ℃. The resulting high-speed supernatant (HSS) was used for later experiments. Pyrenyl-actin was dissolved in column buffer (TEA, 0.3 mM $CaCl_2$, 0.1 mM EDTA, 0.7 mM ATP, and 6.25 mM NaN_3) for 1 hour, spun at 80,000 rpm in a Beckman TLA-100.3 rotor for 20 min at 4 ℃ to remove F-actin, and mixed with Mg^2+ converting buffer for 5 min to convert Ca^{2+}-actin to Mg^{2+}-actin. Mg^{2+}-pyrenl-actin was then diluted in the polymerization buffer (60 mM KCl, 2.5 mM NaCl, 0.6 mM $MgCl_2$, 5 mM Tris-HCl, pH 7.5, 2.5 mM HEPES, pH 7.1, 0.5 mM EGTA, 30 μM $CaCl_2$, 0.2 mM ATP, and 0.3 mM NaN_3) to a final concentration of 1.5 μM and immediately mixed with HSS, which contained 2.4–2.6 μM unlabeled G-actin as estimated by Western blot (data not shown) in the presence of 0.2 mM ATP and 50 nM GST-tagged verprolin, cofilin, and acidic (VCA) domain of mammalian N-WASP. The mixture was quickly transferred into a well of 96-well plate, and the fluorescence intensity was read every 10 s in a Molecular Device SpectraMax Gemini EM plate reader at the wavelength of 365/407 (Ex/Em). Polymerization curves and rates were obtained using Excel (Microsoft). The polymerization rate was represented as the maximal slope of the elongation phase of each curve.

SUPPLEMENTAL REFERENCES

Canham, P.B. (1970). The minimum energy of bending as a possible explanation of the bicon-cave shape of the human red blood cell. J. Theor. Biol. *26*, 61 – 81.

do Carmo, M.P. (1976). Differential geometry of curves and surfaces. (Engelwood Cliffs, New Jersey: Prentice Hall).

Frank, J.R., and Kardar, M. (2008). Defects in nematic membranes can buckle into pseudospheres. Phys. Rev. E. Stat. Nonlin. Soft Matter Phys. *77*, 41705.

Helfrich, W. (1973). Elastic properties of lipid bilayers: theory and possible experiments. Z.Naturforsch. C. *28*, 693-703.

Landau, L.D., and Lifshitz, E.M. (1970). Theory of Elasticity. (Oxford: Pergamon Press).

Lebwohl, P.A., and Lasher, G. (1972). Nematic-liquid-crystal order- a monte-carlo calculation. Phys. Rev. *A6*, 426-429.

Lee, S.H., Kerff, F., Chereau, D., Ferron, F., Klug, A., and Dominguez, R. (2007). Structural basis for the actin-binding function of missing-in-metastasis. Structure *15*, 145-155.

Ramakrishnan, N., Ipsen, J.H., Sunil Kumar, P.B. (2012). Role of disclinations in determining the morphology of deformable fluid interfaces. Soft Matter *8*, 3058–3061.

Ramakrishnan, N., Kumar, P. B. S., Ipsen, J. H. (2013) Curvature mediated oligomerization of curvature inducing nematogens and membrane tubulation, Biophysical Journal *104*, 1-11.

Yang, C., Czech, L., Gerboth, S., Kojima, S., Scita, G., and Svitkina, T. (2007). Novel roles of formin mDia2 in lamellipodia and filopodia formation in motile cells. PLoS Biol. *5*, e317.